JGR Oceans

RESEARCH ARTICLE
10.1029/2020JC016503

Asymmetric Internal Tide Generation in the Presence of a Steady Flow

Yvan Dossmann[1,2], Callum Shakespeare[2], Kial Stewart[2], and Andrew McC. Hogg[2,3]

[1]LEMTA, UMR 7563, Université de Lorraine, CNRS, F-54500, Vandoeuvre-les-Nancy, France, [2]Research School of Earth Sciences, The Australian National University, Canberra, ACT, Australia, [3]ARC Centre of Excellence for Climate Extremes, Sydney, New South Wales, Australia

Key Points:
- The dynamics of topographic internal waves generated by the sum of a steady and oscillatory flow is studied for varying ridge shape
- A topographically controlled asymmetry is measured in the energy fluxes carried by the upstream and downstream IW beams
- The asymmetry and the generation of nonlinear structures impact the distribution of IW-induced mixing in the ocean interior

Correspondence to:
Y. Dossmann,
yvan.dossmann@univ-lorraine.fr

Citation:
Dossmann, Y., Shakespeare, C. J., Stewart, K. D., & Hogg, A. M. (2020). Asymmetric internal tide generation in the presence of a steady flow. *Journal of Geophysical Research: Oceans*, *125*, e2020JC016503. https://doi.org/10.1029/2020JC016503

Received 15 JUN 2020
Accepted 15 SEP 2020
Accepted article online 27 SEP 2020

Abstract The generation of topographic internal waves (IWs) by the sum of an oscillatory and a steady flow is investigated experimentally and with a linear model. The two forcing flows represent the combination of a tidal constituent and a weaker quasi-steady flow interacting with an abyssal hill. The combined forcings cause a coupling between internal tides and lee waves that impacts their dynamics of IWs as well as the energy carried away. An asymmetry is observed in the structure of upstream and downstream IW beams due to a quasi-Doppler shift effect. This asymmetry is enhanced for the narrowest ridge on which a superbuoyancy ($\omega > N$) downstream beam and an evanescent upstream beam are measured. Energy fluxes are measured and compared with the linear model, that has been extended to account for the coupling mechanism. The structure and amplitude of energy fluxes match well in most regimes, showing the relevance of the linear prediction for IW wave energy budgets, while the energy flux toward IW beams is limited by the generation of periodic vortices in a particular experiment. The upstream-bias energy flux—and consequently net horizontal momentum—described in Shakespeare (2020, https://doi.org/10.1175/JPO-D-19-0179.1) is measured in the experiments. The coupling mechanism plays an important role in the pathway to IW-induced mixing, that has previously been quantified independently for lee waves and internal tides. Hence, future parameterizations of IW processes ought to include the coupling mechanism to quantify its impact on the global distribution of mixing.

Plain Language Summary When tides and currents interact with abyssal topographies, such as ridges and hills, they generate internal waves that propagate in the ocean interior. The energy transported by these waves sustains the largest scale oceanic motions. To improve our understanding of how and where energy is transferred to oceanic currents, an important step is to describe the fate of internal waves, from their generation to their breaking. Previous studies have independently described the dynamics of internal waves generated by tides, or by a steady current. Here we combine the two types of currents—a situation that is met at many oceanic sites—using laboratory experiments and a linear model. The combined currents cause an asymmetry in the internal wave structure. Internal waves are more energetic on the upstream side of the ridge, a phenomenon that is amplified when decreasing the ridge width. The measured energy matches the model prediction in all but one experiment. This gap is likely related to the formation of a vertical swirl close to the ridge that limits energy transfers to internal waves. These results contributes to improve our understanding of the internal wave dynamics and to better represent their effects in oceanic models.

1. Introduction

Internal waves (IWs) play an important role in sustaining the meridional overturning circulation (MOC) by inducing a wide range of turbulent mixing processes (Kunze, 2017; MacKinnon et al., 2017; Munk & Wunsch, 1998; Sarkar & Scotti, 2017).

IWs are predominantly generated either at the surface by wind fluctuations or at the ocean bottom by the interaction of flow with topography. Two seemingly independent classes of topographic IWs have been distinguished in previous studies. In regions where strong barotropic tidal flows interact with large-scale topographies, such as the Mid-Atlantic Ridge, IWs are usually organized as propagating beams called internal tides (Buijsman et al., 2014; Gregg & Ozsoy, 1999; Melet et al., 2013; Nycander, 2005, 2006;

Polzin et al., 1997). On the other hand, in regions where a vigorous geostrophic eddy fields interact with smaller-scale topographies such as in the Antarctic Circumpolar Current, IWs are organized as quasi-steady lee waves (Dossmann, Gamble Rosevear, et al., 2016; Nikurashin & Ferrari, 2010a, 2010b; Yang et al., 2018; Zheng & Nikurashin, 2019). The respective contributions of these two classes of IWs to mixing and subsequent water-masses transformation have been assessed independently using the linear theory of Bell (1975) and semiempirical parameterizations (St. Laurent et al., 2002; Polzin, 2009) leading to global estimates maps of IW mixing (e.g., de Lavergne et al., 2020; Falahat et al., 2014; Melet et al., 2013; Nikurashin & Ferrari, 2011, 2013; Nycander, 2005; Vic et al., 2019).

Barotropic tides coexist with quasi-steady flows at many IW generation sites. This observation motivated Shakespeare (2020) to revisit the classical linear IW generation theory of Bell (1975). The combination of a barotropic tidal component and a steady flow causes a linear coupling between internal tides and lee waves that has not been accounted for in previous IW energy budgets. Bell's (1975) theory was extended to include the coupling between multiple flow constituents. A new nomenclature was introduced to distinguish IWs propagating as "free beams" from "flow-trapped" waves that can only propagate in the presence of the flow that supports them.

The extended linear theory predicts major changes in the IW dynamics owing to this coupling that affects the following:

- The energy fluxes to lee waves. Lee wave generation and induced mixing are largely canceled (by up to 90% in some key areas, such as the Drake Passage) and are overestimated by 13–19% on a global scale using the classical approach.
- The generation of internal tides beyond the critical latitudes. Doppler-shifted IW beams can propagate in regions where they would dissipate in the absence of a steady flow, hence modifying the spatial distribution of IWs and subsequent mixing.
- The existence of a net wave stress above abyssal hills. The linear coupling causes an asymmetry between the upstream and downstream internal tide beams generated over hills, which induces a net wave stress of 0.01–0.1 N/m^2 (comparable to the local wind stress).

Several limitations have been put forward by Shakespeare (2020) regarding the application of the classical and extended theory of Bell (1975). First, the model is linear and does not account for finite amplitude effects that induce flow blocking and saturation in the supercritical regime. Second, the large uncertainties on the deep-ocean stratification and geostrophic flows lead to an important variability of IW energy, momentum, and mixing budgets between studies.

The use of laboratory experiments permits exploration of the dynamics of IWs and the pathway to mixing in controlled parameter ranges that are relevant to real oceanic processes (Aguilar et al., 2006; Bourget et al., 2013; Dossmann, Bourget, et al., 2016; Dossmann et al., 2011; Zhang et al., 2007). While the experimental scales are shorter than the oceanic scales, typical values of $10^3 < Re < 5 \times 10^3$) are reached which allow for the development of nonlinear processes leading to the turbulent cascade to mixing scales. In a previous experimental study, both the linear lee wave field predicted by Bell's theory and a complex nonlinear dynamics in the boundary layer were captured using the light attenuation technique (Dossmann, Gamble Rosevear, et al., 2016). Mixing diagnostics showed that boundary layer nonlinear processes, such as flow separation, hydraulic jumps, and turbulent bursts, overcome IW-induced mixing in most ocean relevant parameter regimes, highlighting the need to account for these effects in the mass and energy budgets of the MOC (MacKinnon et al., 2017; Todd, 2017; Zheng & Nikurashin, 2019).

The present work aims to describe the linear dynamics of topographic IWs forced by the combination of an oscillatory flow and a steady flow and to accurately quantify the associated energy flux. It relies on laboratory experiments for which the flow, topography, and background stratification are precisely controlled and the flow dynamics is measured at high space-time resolution. This idealized approach permits direct comparison at the laboratory scale of the energy flux estimated from the extended linear theory against accurate high-resolution measurements in an identical experimental configuration for which both the linear IW dynamics and nonlinear structures—vortices, hydraulic jumps, and partial wave breaking—can develop.

The manuscript is organized as follows. In section 2, the extended linear theory is described and the different IW regimes are introduced. The experimental setup is presented in section 3. The IW dynamics and energy

flux fields are described in sections 4 and 5. Implications for IW energy budgets in the ocean are discussed in section 6.

2. Linear Theory

2.1. Extended Linear Theory

In order to make meaningful comparisons with our experimental results, it is necessary to slightly extend previous models for linear IW generation by flow over topography to simultaneously include (i) finite fluid depth, (ii) both steady and oscillatory background flow, (iii) nonnegligible excursion parameters, (iv) non-hydrostatic dynamics, and (v) a mechanism of dissipation for the waves. The excursion parameters ϵ and $\bar{\epsilon}$ are a measure of the distance traveled by a particle moving with either the steady or the oscillatory flow relative to the topographic length during a tidal period. As such, the theory here can be thought of as generalizing that of Bell (1975) and Shakespeare (2020) to include finite-depth and wave dissipation or the theory of Shakespeare et al. (2020) to include nonnegligible excursion parameters.

Here, the background flow of interest is a combined steady and oscillatory flow: $\boldsymbol{U} = \boldsymbol{U}_c + \boldsymbol{U_0}\cos\omega t$, where ω is the forcing frequency and t is time. For completeness, we will include a nonzero Coriolis parameter f and three-dimensionality in the following. The simplest starting point for our derivation is the linearized wave equations including a zeroth order drag parameter α as introduced in equation 19 of Shakespeare et al. (2020):

$$\frac{\bar{D}}{Dt}\mathbf{u'} + f\hat{\mathbf{z}} = -\nabla p' + b'\mathbf{z} - \alpha\mathbf{u'}_h, \tag{1a}$$

$$\nabla \cdot \mathbf{u'} = 0, \tag{1b}$$

$$\frac{\bar{D}}{Dt}b' + N^2 w' = -\alpha b', \tag{1c}$$

where

$$\frac{\bar{D}}{Dt} = \frac{\partial}{\partial t} + \boldsymbol{U}_c \cdot \nabla, \tag{2}$$

and $\mathbf{u'} = (u', v', w')$, $\mathbf{u'}_h$, b', and p' are the total velocity, horizontal velocity, buoyancy, and pressure perturbations. Wave generation occurs at the ocean bottom ($z = -H$) and a rigid-lid boundary condition is set at the ocean surface ($z = 0$). Introducing the Fourier transform in the horizontal coordinates x and y for perturbation fields

$$w' = Re[\hat{w'}\exp(-i(kx + ly + \omega t))], \tag{3}$$

one obtains

$$\left[\frac{\partial^2}{\partial z^2} + \frac{K^2(N^2 - \omega^2 - i\alpha\omega)}{\omega^2 - (f^2 + \alpha^2) + 2i\alpha\omega}\right]\hat{w'} = 0. \tag{4}$$

For a given harmonic n, the Fourier transforms of w' and p' are given by

$$\hat{w}_n = \hat{w}_n|_{-H}\frac{e^{-imz-\gamma z} - e^{imz+\gamma z}}{e^{imH+\gamma H} - e^{-imH-\gamma H}}, \tag{5a}$$

and

$$\hat{p}_n = -\frac{N^2 - \omega_n^2}{m\omega_n}\hat{w}_n|_{-H}\frac{e^{-imz-\gamma z} + e^{imz+\gamma z}}{e^{imH+\gamma H} - e^{-imH-\gamma H}}, \tag{5b}$$

where

$$m = \mathrm{sgn}(\omega_n)K\sqrt{\frac{N^2 - \omega_n^2}{\omega_n^2 - f^2}}, \tag{5c}$$

is the vertical wavenumber, $K = \sqrt{k^2 + l^2}$ is the horizontal wavenumber modulus, and

$$\gamma = \alpha m \frac{\omega_n(2N^2 - \omega_n^2 - f^2)}{2(N^2 - \omega_n^2)(\omega_n^2 - f^2)}, \tag{5d}$$

is the decay rate of wave amplitude per unit wavelength, with $\gamma \ll m$ for valid solutions. The magnitude of this decay rate is determined by the Rayleigh drag α (in inverse seconds) and represents wave damping by instabilities, breaking, and wave-wave interactions—this damping is used as a purely numerical tool herein, as will be explained below.

Equation 5d may be generalized to include steady and tidal flows, and large excursion distances, by summing over intrinsic frequencies for each harmonic:

$$\omega_n = n\omega + \boldsymbol{k} \cdot \boldsymbol{U}_c, \tag{6}$$

where n is the harmonic number and the Fourier transform in x and y of the total vertical velocity is thus

$$\hat{w}(k, l, z, t) = \sum_{n=-\infty}^{\infty} \hat{w}_n e^{i\omega_n t}, \tag{7}$$

and similarly for pressure. The bottom boundary condition on the vertical velocity, associated with the no-normal flow condition, that is, $w = \boldsymbol{U} \cdot \boldsymbol{\nabla} h$ for topographic height h in the small amplitude approximation, gives

$$\hat{w}_n|_{-H} = i\omega_n \hat{h} J_n\left(\frac{\boldsymbol{k} \cdot \boldsymbol{U}_0}{\omega}\right), \tag{8}$$

where J_n is the order n Bessel function of the first kind (see, e.g., Bell, 1975; Shakespeare, 2020).

The solution in this form is expressed in a coordinate frame $\boldsymbol{x_0}$ *following the total flow* $\boldsymbol{U}$ (i.e., $\boldsymbol{x} = \boldsymbol{x_0} + \int_0^t \boldsymbol{U}\, dt'$ where $\boldsymbol{x}$ is the Eulerian position and $\boldsymbol{x_0}$ the flow-following coordinate). We use the above solutions to compute the theoretical energy flux as a function of time and space via

$$F(x, y, z, t) = \mathcal{F}^{-1}[\hat{w} e^{-i\boldsymbol{k}\cdot\boldsymbol{U}_c t}]\mathcal{F}^{-1}[\hat{p} e^{-i\boldsymbol{k}\cdot\boldsymbol{U}_c t}], \tag{9}$$

where $\mathcal{F}^{-1} = 1/(4\pi^2)\int\int e^{-i(kx+ly)} dk\, dl$ denotes the inverse Fourier transform. To calculate these inverse Fourier transforms numerically, the vertical velocity and pressure fields must decay toward the boundaries of the (numerical) domain; otherwise, the waves continuously wrap around and the numerical solution is meaningless. The decay of the wavefields is ensured by turning the Rayleigh drag α in Equation 5d to a sensible value.

2.2. IW Regimes

Four IW regimes are expected due to the combination of a steady and an oscillatory forcing flow. The linearization of Euler's equation under the Boussinesq approximation leads to the following dispersion relation for IWs:

$$\tilde{\omega}^2 = N^2 \sin\theta^2 + f^2 \cos\theta^2, \tag{10}$$

with $\tilde{\omega} = \omega - \boldsymbol{k} \cdot \boldsymbol{U_c}$, N, and f the intrinsic IW frequency, the Brunt-Väisälä frequency, and the local Coriolis parameter. Here, ω is the frequency of the oscillatory flow, $\boldsymbol{k} \cdot \boldsymbol{U_c}$ is a quasi-Doppler frequency shift induced by the steady flow $\boldsymbol{U_c}$ onto the IW of horizontal wavenumber $\boldsymbol{k}$, and θ is the angle of the group velocity with respect to the horizontal. In fact, the presence of a steady flow does not imply a Doppler shift in the strict sense as extensively argued by Gerkema et al. (2013). Equation 10 implies that $f < |\tilde{\omega}| < N$ for propagating IWs. Depending on the signs of $|\boldsymbol{k} \cdot \boldsymbol{U_c}|/\omega$ (the dot product of the inverse wave phase speed and the steady flow velocity) and $\tilde{\omega}$, four nonevanescent bands are allowed: lee waves, upstream and downstream beams, and tidal lee waves. The four bands are represented in Figure 1a in the nonrotating case.

The first nonevanescent band, indicated by the solid red line in Figure 1a, corresponds to the classical lee wave generation by the steady forcing ($\omega = 0, f < |\boldsymbol{k} \cdot \boldsymbol{U_c}| < N$) downstream of the steady flow.

There are two nonevanescent bands (blue shaded areas in Figure 1a) with positive intrinsic frequencies $\tilde{\omega} > 0$, one in the upstream direction ($\boldsymbol{k} \cdot \boldsymbol{U_c}/\omega < 0, f - |\boldsymbol{k} \cdot \boldsymbol{U_c}| < \omega < N - |\boldsymbol{k} \cdot \boldsymbol{U_c}|$) and one in the downstream

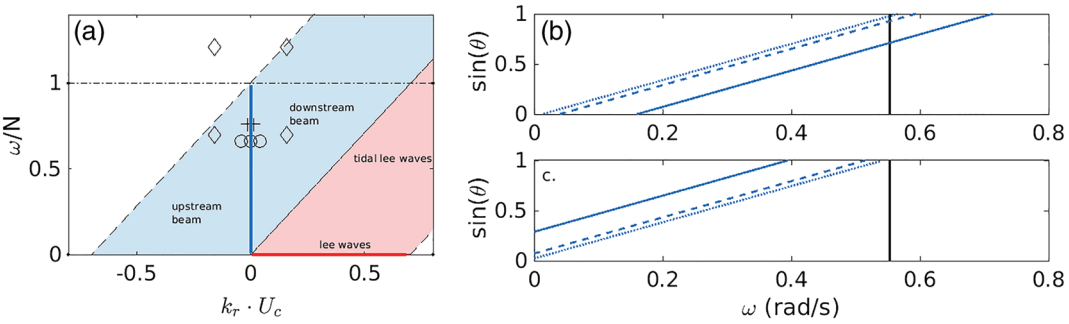

Figure 1. (a) Regimes diagram for internal waves in the presence of an oscillatory and a steady forcing flow. The blue line and the blue shaded area are the nonevanescent bands for pure internal tides and free beams. The red line and the red shaded area are the nonevanescent bands for lee waves and tidal lee waves. The symbols ◇, ○, and + show the experiments with Ridges A–C, respectively. (b and c) Linear dispersion relations for internal waves in the presence of a steady flow for the downstream (b) and upstream beams (c) for Ridges A (solid), B (dashed), and C (dotted).

direction ($\boldsymbol{k} \cdot \boldsymbol{U_c}/\omega > 0, f + |\boldsymbol{k} \cdot \boldsymbol{U_c}| < \omega < N + |\boldsymbol{k} \cdot \boldsymbol{U_c}|$). In these two bands, the IW field is organized as beams propagating upstream and downstream of the flow. The dispersion relation for the downstream and upstream beams are shown in Figures 1b and 1c for the three experimental ridges. In particular, IWs are able to propagate in regions where $\omega > N$ (superbuoyancy downstream beam) or $\omega < f$ (subinertial upstream beam).

In the downstream direction, nonevanescent IWs with $\tilde{\omega} < 0$ are allowed in the band $|\boldsymbol{k} \cdot \boldsymbol{U_c}| - N < \omega < |\boldsymbol{k} \cdot \boldsymbol{U_c}| - f$ (red shaded areas in Figure 1a). In this band, IWs are organized as a steady lee wave field at larger wavenumber than classical lee waves and that only exists in the presence of a barotropic tide. The term tidal lee waves was introduced by Shakespeare (2020) to refer to this IW regime.

Three of the four IW regimes generated by the combination of a steady and an oscillatory flow are shown in Figure 2 using the extended linear model described in the previous section. The two forcing flows are artificially uncoupled in Figure 2a, in which one identifies the generation of symmetrical internal tidal beams on either side of the ridge as well as lee waves. Turning on the coupling leads to more complex dynamics. The symmetry between the upstream beam and the downstream beam is broken by the presence of the steady flow as will be discussed in section 4. Lee waves are still generated on the downstream side, but their amplitude is weakened by the coupling mechanism. For the chosen forcing parameters, the generation of tidal lee waves is limited by the relatively small value of the steady flow, as will be the case in the experiments.

In this work experiments are performed in a nonrotating, strongly stratified flow. The effects of rotation on the IW dynamics are neglected on the experiment time scale. The dispersion relation (10) can therefore be simplified to $\omega = N \sin(\theta) - |\boldsymbol{k} \cdot \boldsymbol{U_c}|$ for the upstream beam and $\omega = N \sin(\theta) + |\boldsymbol{k} \cdot \boldsymbol{U_c}|$ for the downstream beam, as shown in Figure 1. The mean excursion distance parameter $\bar{\epsilon} = |\boldsymbol{k} \cdot \boldsymbol{U_c}|/\omega$ is introduced to quantify the relative magnitude of the quasi-Doppler shift and hence the asymmetry between the upstream and

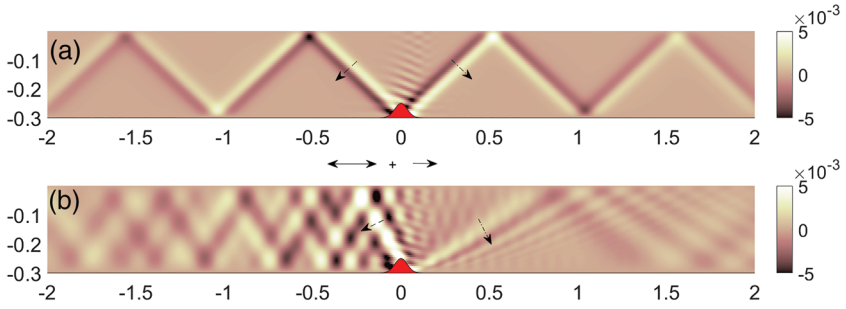

Figure 2. Vertical velocity (m/s) field for internal wave generation over a Gaussian ridge using the extended linear theory of Bell (1975) for independent (a) and coupled (b) forcings. The solid arrows show the relative magnitude of the oscillatory (2 cm/s) and steady (0.4 cm/s) flows. The dashed and dash-dotted arrows indicate the phase propagation in the upstream and downstream beams. The topography is shown shaded in red.

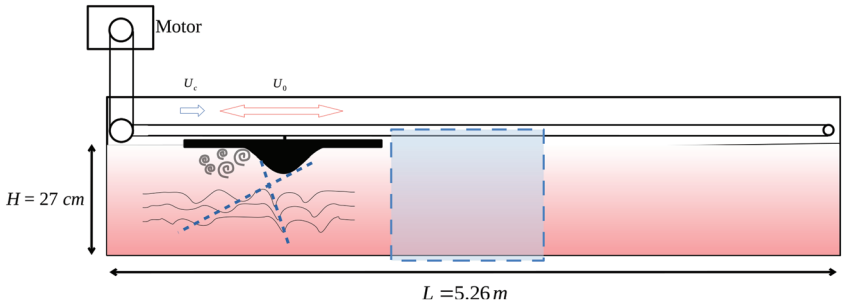

Figure 3. Sketch of the experimental apparatus. The tank is filled using the double-bucket technique with a linearly stratified fluid. The step motor is computer controlled to impose a steady (blue arrow) and oscillatory (red arrow) forcing motion to the ridge in Experiments II–V, which generates internal wave beams in the body of the flow. The steady motion is set to 0 in Experiment I. The blue rectangle indicates the measurement area for the light attenuation technique.

downstream beams. The beam horizontal wavenumber is scaled by the topographic width. Hence, the asymmetry between the upstream and downstream beams is expected to be enhanced for strong steady flows impinging on smaller-scale topographies.

The series of experiments aims to describe the IW field induced by the combined forcings and the effect of the asymmetry on the transported energy fluxes.

3. Experimental Setup

3.1. Apparatus

Experiments have been performed in a 5.26 m long, 20 cm wide, and 40 cm high Perspex tank in the Geophysical Fluid Dynamics laboratory at the Australian National University. The air temperature is controlled at 20 ± 1°C. The experimental setup is sketched in Figure 3. The tank is filled with the double-bucket technique using two drums, one initially filled with brine and the other with freshwater. The drums are filled with hot water to allow an efficient salt dissolution. A fixed volume of 10 ml of red food dye is added to the drum filled with brine. It is used as a passive tracer for salinity as described in the following subsection. The tank is filled to a height of $H \approx 27$ cm in approximately 3 hr using two floating devices. The slow flow rate allows a linear stratification to be obtained over the fluid depth, while shallow mixed layers of less than 1 cm are observed close to the tank bottom and free surface, due to boundary exchanges. In most fills the two drums have been prepared 24 hr before the start of the fill to achieve temperature equilibrium between water and air. Several fills have been carried out with water hotter than air, which led to the formation of double diffusive layers. These layers had no visible impact on the IW dynamics and permitted observation of the interfacial displacement using the shadowgraph technique in qualitative experiments. For most experiments, a constant Brunt-Väisälä frequency $N_0 = 0.7$ rad/s is set, with $N_0 = \sqrt{-g/\rho_0 \times d\bar{\rho}/dz}$. $g = 9.81$ m/s^2, $\rho_0 = 1000$ kg/m^3, $\bar{\rho}$, and z are the gravity, the reference density, the density profile, and the vertical coordinate with the origin at the tank bottom, respectively.

The forcing is performed by towing a bidimensional ridge of Gaussian shape over the length of the tank, at the free surface of the fluid. The ridge profile is given by

$$h(x) = h_0 \exp\left(-\left(k_r x\right)^2\right), \tag{11}$$

where x is the horizontal coordinate with the origin at the center of the ridge base, $h_0 = 3.5$ cm is the ridge height and k_r is the characteristic horizontal wavenumber. Experiments have been performed with three different ridges of varying e-folding width $l_r = 1/k_r = 1.5$ cm (Ridge A), $l_r = 5$ cm (Ridge B), and $l_r = 16$ cm (Ridge C). The ridges are attached to an 80 cm long plate to allow for boundary layers to develop during motion. The weight of the plate is adjusted so that the ridge is completely submerged, and the flat section of the plate lies a few millimeters below the free surface. The ridge motion is controlled by a Smartmotor interface via a wire attached to a rotating cylinder. The program independently controls a steady and an oscillatory rotation of the cylinder, which respectively impose a constant velocity U_c and an oscillatory velocity $U_0 \cos(\omega t)$ to the ridge. The ridge transits 1 to 20 times over the length of the tank during an experiment. The flow is decelerated/accelerated over 30 cm close to the end walls to ensure a continuous forcing velocity.

Table 1
Experimental Parameters

Experiment	U_c (cm/s)	U_0 (cm/s)	Ridge	ω/N	$\bar{\epsilon}$
I	0	2	B	0.66	0
II	0.2	2	B	0.66	0.09
III	0.2	2	A	0.70	0.36
IV	0.2	2	A	1.21	0.20
V	0.2	2	C	0.76	0.03

Note. The experiment is carried out several times to vary the duration of forcing sequences. The latter are separated by resting sequences to allow for measurements of the background stratification.

Hence, this configuration permits the simulation of the combined effects of a steady flow and a barotropic tide interacting with an oceanic ridge. The relative magnitude of the two forcings and the tidal period can be adjusted to reach a parameter space relevant for oceanic configurations. The initially linear stratification represents the regular density gradient in the deep ocean.

In total, 14 fills have been performed during the experimental campaign, for which the forcing parameters were varied.

Five selected experiments showing different aspects of the asymmetric generation of free beams—which are the main source of IW energy transport over hills apart from the Southern Ocean—are discussed in the following sections. Table 1 and Figure 1a summarize the relevant parameters of the experiments.

3.2. Light Attenuation Technique

The light attenuation technique infers local density from absorption measurements at high spatial resolution (Allgayer & Hunt, 1991; Hacker et al., 1996; Sutherland et al., 2012). This method has previously been used to describe the dynamics of IWs generated in the lee of a moving topography as well as the induced mixing (Dossmann, Gamble Rosevear, et al., 2016).

The light absorption $A(x,z,t) = \log(I_0(x,z)/I(x,z,t)$ due to the red food dye is measured using the intensity field from a reference image $I_0(x,z)$ and from an image recorded in the course of the experiment $I(x,z,t)$. The initial concentration of red dye is chosen such that the absorption law is in the linear (Beer-Lambert) regime: $A = \epsilon_\lambda Wc$, where ϵ_λ, W, and c are the extinction coefficient for the red component of the camera sensor, the tank width and the dye concentration.

A calibration is applied using two density samples from the flow to eventually convert absorption values to cross-tank averaged density anomalies $\Delta\rho(x,z,t)$ at each pixel. A median filter is applied over 10 pixels in the two directions to remove measurement noise. The reader can refer to Dossmann, Gamble Rosevear, et al. (2016) for a detailed description of the light attenuation technique. A LED panel of dimensions 100 cm × 60 cm is placed to illuminate to central part of the tank. Images are recorded in RAW format at 14 bits using a Nikon D300 Reflex camera equipped with a 200 mm telephoto lens. The camera is placed approximately 6 m away from the tank to minimize parallax effects.

4. IW Dynamics

In this section we investigate the dynamics induced by the flow/ridge interaction for varying the mean excursion distance parameter $\bar{\epsilon}$ and forcing frequency ω/N. The experiments are designed to put forward the role of the quasi-Doppler shift on the IW dynamics. The ridge oscillates at the same velocity amplitude $U_0 = 2$ cm/s and similar forcing frequency $\omega/N \sim 0.7$ in Experiments I–III and V. In the Reference Experiment I, the forcing consists of a purely oscillatory flow generating internal tides. In Experiments II–V, the ridge of varying width is moving rightward at a constant velocity $U_c = 2$ mm/s, which represents a leftward steady flow. Hence, the downstream (upstream) region is on the left (right) side of the ridge. As the

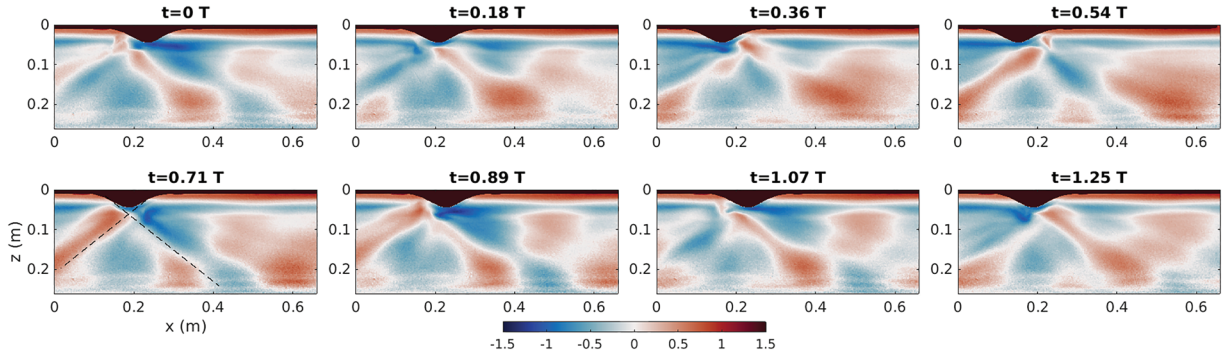

Figure 4. Experiment I: Density anomaly field $\Delta\rho$ (kg/m)^3 ($U_c = 0$ cm/s, $U_0 = 2$ cm/s, and $\omega/N = 0.66$, Ridge B). The dashed lines show the beam angles predicted by linear theory.

quasi-Doppler shift is controlled by the horizontal wavenumber scaled by the ridge, the asymmetry between the upstream and downstream beams is therefore expected to increase for increasing k_r (Experiments V, II, and III).

The setup of Experiment IV is the same as in Experiment III, except that the forcing frequency is increased to $\omega/N = 1.21$. This particular experiment is likely to show a strong asymmetry in the IW dynamics, as the regime diagram predicts the generation of a downstream—superbuoyant—IW beam and no evanescent IW on the upstream side.

In the absence of the steady forcing flow ($\bar{\epsilon} = 0$) the generation of symmetrical IW beams on the two sides of the ridge is measured in Experiment I (Figure 4). The beams are in phase opposition, and their angle matches the expected angle from the linear dispersion relation. The high mode IW field is superimposed on a background wavefield likely due to fast propagating low modes reflecting at the tank walls.

The steady flow is then turned on in Experiment II ($\bar{\epsilon} = 0.09$), for the same ridge and forcing frequency as in Experiment I (Figure 5). The generation of sharp beams occurs on both sides of the ridge with an important asymmetry between the upstream and downstream beams. The upstream beam shows a larger amplitude and is steeper than the downstream beam. The linear prediction of the beam angles including the steady flow is shown by the dashed lines in Figure 5. Both beam angles match the linear dispersion relation. The slow rightward ridge motion induces the periodic formation of a vortex on the lee side of the ridge as seen at $t = 0.71T$ (circled). This vortex only forms in the phase when the steady and tidal flows are in the same direction and is likely to contribute to mixing in the vicinity of the ridge.

Decreasing the ridge width in Experiment III leads to a larger value of $\bar{\epsilon} = 0.36$ (see Figure 6). Again, sharp IW beams form periodically on the two sides of the ridge, with a larger angle difference between the upstream and downstreams beams than in Experiment II. Contrary to Experiment II, no vortex is observed close to the ridge. This indicates that the generation of this nonlinear structure in the boundary layer is dependent on the shape of the topography.

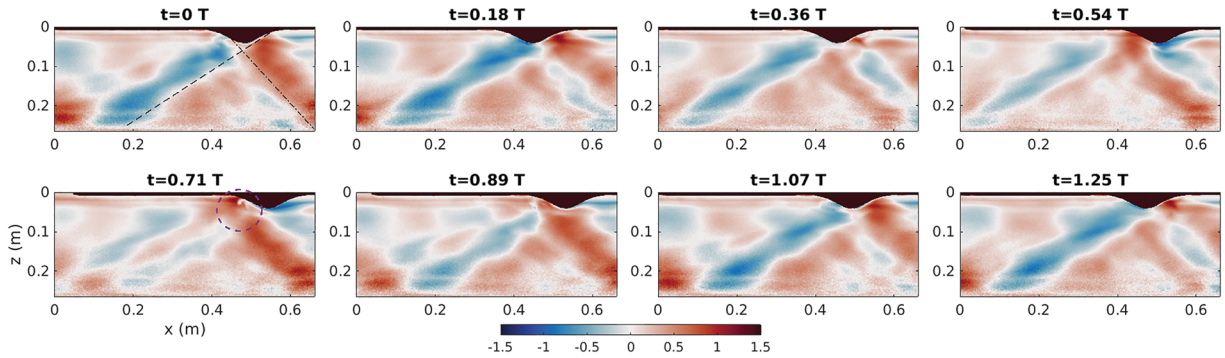

Figure 5. Experiment II: Density anomaly field $\Delta\rho$ (kg/m)^3 ($U_c = 0.2$ cm/s, $U_0 = 2$ cm/s, and $\omega/N = 0.66$, Ridge B). The steady ridge motion is to the right of the field. The dashed lines show the beam angles predicted by linear theory. The formation of a vortex on the downstream side of the ridge is shown by the purple dashed circle at $t = 0.71$ T.

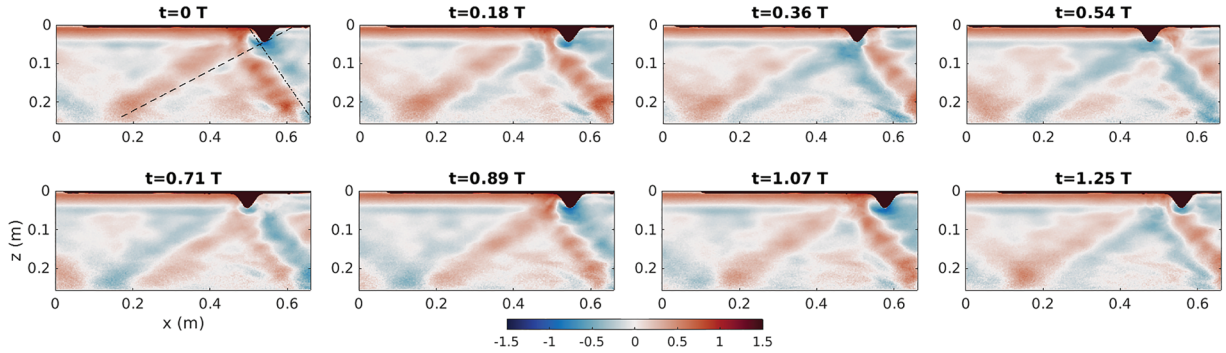

Figure 6. Experiment III: Density anomaly field $\Delta\rho$ (kg/m)^3 ($U_c = 0.2$ cm/s, $U_0 = 2$ cm/s, and $\omega/N = 0.70$, Ridge A). The dashed lines show the beam angles predicted by linear theory.

The generation of a superbuoyant IW beam—that is, an IW beam for which the forcing frequency ω exceeds the background Brunt-Väisälä frequency—is observed in experiment IV ($\bar{\epsilon} = 0.20$ and $\omega/N = 1.21$, Figure 7). The quasi-Doppler shift induced by the steady flow interacting with a sufficiently narrow ridge allows the propagation of this beam on the downstream side on the ridge, while evanescent waves remain on the upstream side as predicted by the regime diagram in Figure 1a. The superbuoyant IW beam interferes with supercritical IW beams that are likely generated by nonlinear effects.

The asymmetry between the upstream and downstream dynamics is illustrated with on horizontal space-time diagrams measured at middepth for Experiments II—IV in Figure 8. The larger amplitude and shorter wavelength of the upstream beam are clearly visible in Experiments II and III. In Experiment IV, the periodic density anomalies do not propagate on the upstream side (as shown by the absence of slope in the space-time diagram), while the subcritical downstream beam and a supercritical beam propagate on the downstream side.

Finally, the ridge width is increased to the largest value of 16 cm in Experiment V, while keeping the same steady velocity and forcing frequency as in Experiments I–III (Figure 9). Hence, the mean excursion parameter $\bar{\epsilon} = 0.03$ is small relative to previous experiments, and one expects a weak asymmetry between the downstream and upstream sides. In fact, periodic density anomalies with a horizontal scale comparable to l_r are generated by the ridge motion. These anomalies appear to be dominated by propagating low modes—by contrast with the sharper beams in Experiments I–IV. No asymmetry in the beams is measured in this experiment.

5. Energy Flux

The measured asymmetry between the upstream and downstream beams impacts the energy fluxes, $\mathbf{J}(x, z, t) = p\mathbf{v}$, carried by IWs and eventually the induced mixing, where $p(x, z, t)$ and $v(x, z, t)$ are the pressure and velocity fields, respectively. The direct measure of energy fluxes remains an experimental challenge as

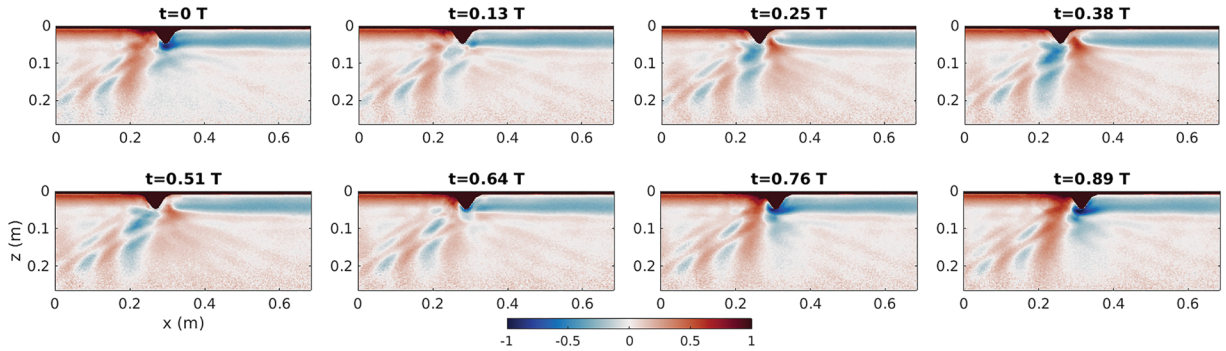

Figure 7. Experiment IV: Density anomaly field $\Delta\rho$ (kg/m)^3 ($U_c = 0.2$ cm/s, $U_0 = 2$ cm/s, and $\omega/N = 1.21$, Ridge A).

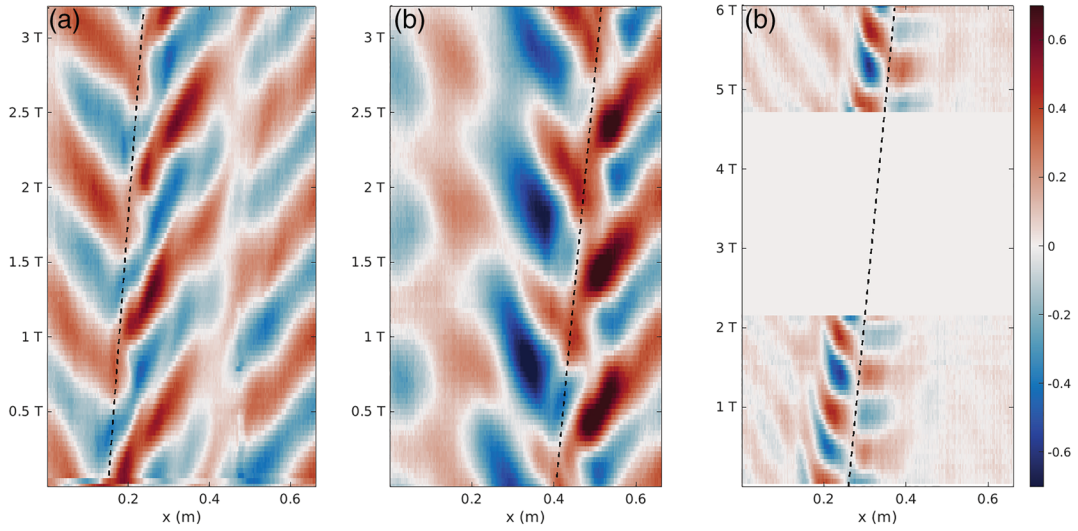

Figure 8. Density anomaly space-time diagrams at middepth for Experiments III (a), II (b), and IV (c). The dashed lines indicate the movement of the ridge due to the steady motion. The whitespace in (c) is where data are unavailable due to the limited camera buffer.

it relies on the simultaneous measurements of the pressure and velocity fields. While it is possible to perform simultaneous measurements of velocity fields with other fields related to density and their derivatives to assess buoyancy fluxes, the authors are not aware of an experimental technique to directly measure the pressure anomaly field.

The method developed by Allshouse et al. (2016) and Lee et al. (2018) is applied to extract the linear energy flux radiated away by IW beams. In this method the pressure field is calculating from a Green's function method using the density anomaly field, while the velocity field is obtained by integrating the continuity equation using the incompressibility assumption. This method was tested on experimental Schlieren data which provide density gradient fields that are then integrated to obtain density anomalies. Agreement with Navier-Stokes simulations was obtained for small-amplitude IW field. In the present work the density anomalies are directly measured from the light attenuation technique, which suppresses the spatial integration step. Instantaneous energy fluxes are calculated using the Matlab GUI EnergyFlux introduced by Allshouse et al. (2016). Their mean contribution is postprocessed and compared with the energy fluxes calculated from the extended linear theory described in section 2.1 (Figure 10).

When no steady flow is present, the energy flux is focused in the symmetrical beams generated on either side of the ridge (Experiment I, Figures 10a and 10d). The predicted and experimental flux fields closely match in amplitude and direction. Adding a steady flow leads to an asymmetry in both the shape and the amplitudes of the energy carried away by the beams as described in section 4. In both Experiments II ($\bar{\epsilon} = 0.36$, Figures 10c and 10f) and III ($\bar{\epsilon} = 0.09$ Figures 10b and 10e), the steady flow increases the energy flux in the upstream

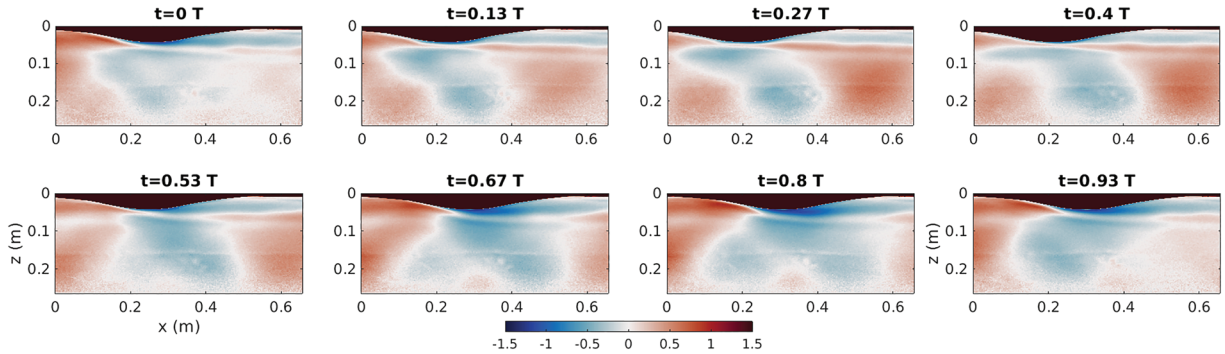

Figure 9. Experiment V: Density anomaly field $\Delta\rho$ (kg/m)^3 ($U_c = 0.2$ cm/s, $U_o = 2$ cm/s, and $\omega/N = 0.76$, Ridge C).

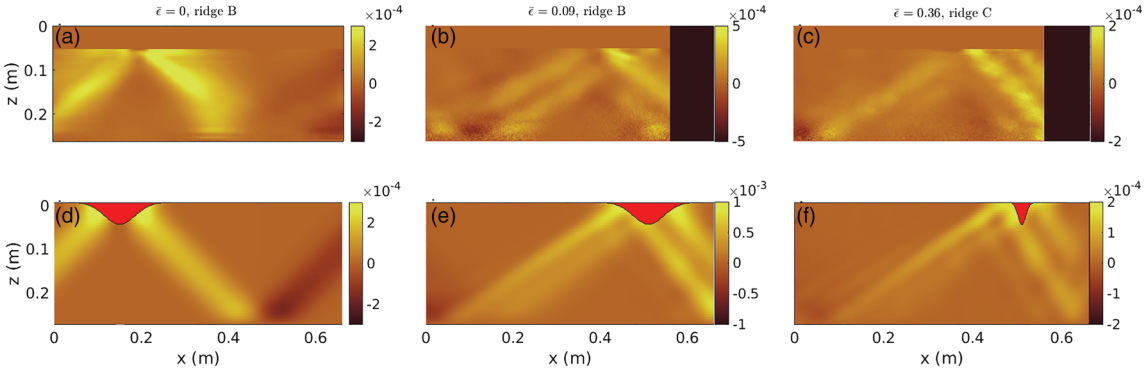

Figure 10. Mean energy fluxes measured in the experiments (top panels) and assessed from the extended Bell's theory (bottom panels) for Experiment I (a and d), Experiment II (b and e), and Experiment III (c and f).

beam relative to the downstream beam. The experimental beam amplitudes are twice as large in Experiment II (Ridge B) as in Experiment III (Ridge C), showing the strong topographic control exerted by the ridge slope on the energy fluxes. The theoretical and experimental amplitudes are similar in the narrower ridge Experiment III; however, the linear energy fluxes are overestimated by a typical factor of 2 in Experiment II. A plausible explanation for this overestimation is that other nonlinear processes are at play in Experiment II that lead to a saturation in the energy fluxes carried away by the linear IW beams. This explanation is consistent with the observation of a vertical vortex generated every tidal period in Experiment II (Figure 5).

A visible beam doubling appears in both the predicted and experimental mean fluxes when measured in the Eulerian frame (Experiments II and III) owing to the relatively large value of the tidal excursion parameter. When measured in the cotidal frame, the mean energy flux is focused in a single beam as shown for Experiment I.

6. Discussion

The combination of a steady flow and an oscillatory flow impinging upon topography leads to the generation of IWs on both sides of the ridge in all selected experiments, except for Experiment IV in which the quasi-Doppler shift prevents the generation of upstream IWs. The latter case is one where downstream IWs are "flow-trapped" as they can only propagate in the presence of the steady flow (see the discussion of Shakespeare, 2020). In Experiments I–III IWs are organized as propagating "free beams" that are modified by the steady flow but would still propagate if the steady flow were canceled. These waves are asymmetric in their direction of propagation, their amplitude, and their wavelength. The asymmetry is increased by increasing the magnitude of the steady flow and by decreasing the ridge width. The beam angles agree well with the extended dispersion relation, including a quasi-Doppler shift, showing that these IWs propagate in a linear fashion. All experiments were performed in regimes where the IW field is dominated by propagating upstream and downstream beams relative to lee waves owing to the small values of the steady flow. Hence, the signature of lee waves is not visible in the density anomalies nor in the energy fluxes.

The processed energy flux fields are successfully compared against the extended linear theory described in section 2.1. The presence of a steady flow induces a larger amplitude and greater energy flux in the upstream beam compared with the downstream beam. The quasi-Doppler shift leads to a more efficient barotropic to baroclinic conversion as the upstream beam approaches the near-critical regime described in Dossmann et al. (2011), while the downstream beam slope flattens. The measured asymmetry confirms the larger integrated energy fluxes measured on the upstream side of ocean ridges and consequently the existence of a net wave stress over abyssal hills proposed in Shakespeare (2020), noting that these experiments are performed in a limited framework compared with the ocean (nonrotating, single tidal forcing). In particular, including rotation would allow for the generation of subinertial upstream beams in the presence of a steady flow. Partial cancelation of the energy flux is expected when including multitidal forcing. Future experiments will focus on quantifying this cancelation by superimposing several tidal components in the oscillatory flow.

The steady flow amplitude is too weak to observe the generation of nonlinear boundary layer structures (hydraulic jump and topographic blocking) described in Dossmann, Gamble Rosevear, et al. (2016). However,

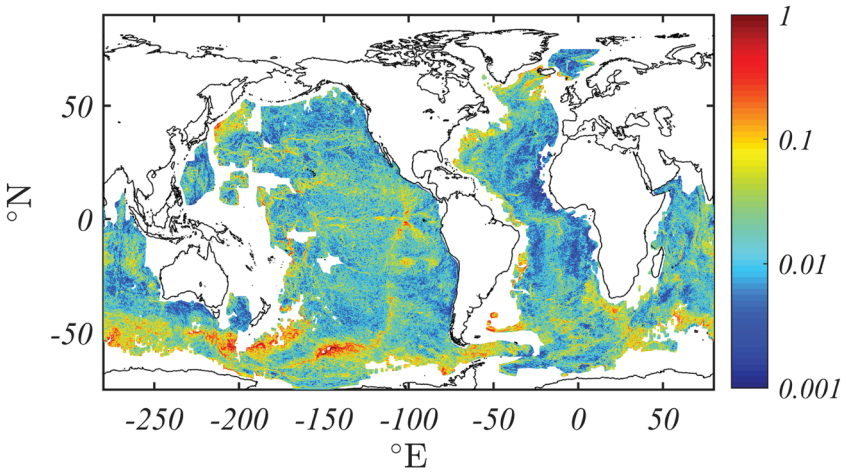

Figure 11. Mean excursion distance parameter $\bar{\epsilon} = k \times U_c/\omega_{M2}$ for the M2 tidal frequency, where k is the abyssal hill cutoff wavenumber. The steady near-bottom velocity U_c is obtained from 5 day averaged near-bottom velocities issued from the ACCESS-OM2-01 0.1^0 resolution global ocean-ice model (Kiss et al., 2020). Abyssal hill topography is sourced from Goff (2010).

the coupling between the steady and oscillatory flows leads to the generation of periodic vortices that are likely to participate to mixing close to the topography and limit the energy transfer toward IW beams. The conditions for the generation of these vortices and their contribution to mixing relative to IWs will be investigated in a companion experimental study.

The pathway to IW-induced mixing in the ocean is likely to be affected by the coupling between the steady flow and the oscillatory flow. IW mixing processes are classified as either far field or near field, depending whether the IW energy escapes the generation site as propagating low modes and dissipates elsewhere or is dissipated in the vicinity of the topography through the breaking of higher mode IWs. The various routes for far-field and near-field IW dissipation are reviewed by MacKinnon et al. (2017), de Lavergne et al. (2019), and de Lavergne et al. (2020).

Low mode IWs, generated by large-scale topography (order 100 km) are apparently unaffected by the presence of a steady flow, as illustrated in Experiment V and consistent with theory predicting a weak quasi-Doppler shift at small wavenumber k_r. However, the remote breaking process of these waves involves a direct cascade of energy through scattering by topography, breaking at continental slopes, interactions with mesoscale steady flows and eddies (Dunphy & Lamb, 2014), and wave-wave interaction through parametric subharmonic instability (MacKinnon et al., 2013). These mechanisms induce IWs at larger wavenumber that can be subject to the quasi-Doppler shift in the presence of a steady flow or other tidal constituents. The role of the quasi-Doppler shift in the pathway to mixing for low mode internal tides is yet to be investigated.

For high mode IWs generated at smaller-scale abyssal hills of order 10 km, the IW field is directly affected by the quasi-Doppler shift as seen in Experiments II–IV.

The dominant sites for generation of high modes internal tides at abyssal hills are the mid-ocean ridges in the Atlantic and western Indian Oceans. At these sites, the asymmetry is particularly favored by the combination of the large topographic roughness of order 10 km, an efficient barotropic to baroclinic conversion of the M2 tide, and the existence of a steady flow. In fact, a global map of the mean excursion distance parameter shows that $\bar{\epsilon} \approx 0.1$ around mid-ocean ridges (Figure 11), which is the range for asymmetric IW beam in the present experiments.

Several processes are likely to be involved in transfer of energy to the scales of mixing directly above the topography, such as interactions with a background IW field, convective instability (Buhler & Muller, 2009), and the parametric subharmonic instability. The mixing efficiency of these mechanisms is controlled by the amplitude and wavenumber of the IW beams (e.g., Bourget et al., 2013; Joubaud et al., 2012).

The present work and Shakespeare (2020) (their Figures 7 and 11) show that IWs are enhanced on the upstream side of abyssal hills. This asymmetry induces a net momentum flux above abyssal hills discussed by Shakespeare (2020) and may alter the efficiency of near-field mixing processes.

On the other hand, in regions of the Southern Ocean where strong quasi-steady flows interact with abyssal roughness, as shown by the red patches in Figure 11, the generation of lee waves is likely to be locally canceled in specific areas due to the interaction with the M2 forcing flow as in the Drake Passage.

In recent works, new process-dependent parameterizations of mixing have been proposed to represent the 3-D distribution of mixing both in the near field and in the far field (relative to IW generation sites) using Lagrangian beam tracing from sources to sinks (de Lavergne et al., 2019, 2020). Four dissipative processes have been identified, including the generation of high mode IWs at abyssal hills. The authors produced global maps of internal tide dissipation by summing the independent contributions of the three main tidal components (M2, S2, and K1). The coupling between these tidal constituents and with the steady flow is not accounted for but is likely to affect the geography of IW sources—by the partial energy transfers between different tidal components—and sinks—by modifying the path taken by IW beams to their breaking site. Consequently, the role played by the coupling process on the global distribution of mixing is a key property to investigate with the proposed parameterizations.

Data Availability Statement

Readers can access the supporting data and linear model via an online repository available at https://doi.org/10.5281/zenodo.3889612 (Dossmann et al., 2020).

Acknowledgments
This work was supported partly by the French PIA project Lorraine Université d' Excellence, reference ANR-15-IDEX-04-LUE. Y. D. acknowledges support from the Embassy of France in Australia. C. J. S. acknowledges support from an ARC Discovery Early Career Researcher Award DE180100087 and ANU Futures Scheme award.

References

Aguilar, D. A., Sutherland, B. R., & Muraki, D. J. (2006). Laboratory generation of internal waves from sinusoidal topography. *Deep Sea Research Part II: Topical Studies in Oceanography*, *53*(1–2), 96–115.

Allgayer, D. M., & Hunt, G. R. (1991). On the application of the light-attenuation technique as a tool for non-intrusive buoyancy measurements. *Experimental Thermal and Fluid Science*, *38*, 257–261.

Allshouse, M. R., Lee, F. M., Morrison, P. J., & Swinney, H. L. (2016). Internal wave pressure, velocity, and energy flux from density perturbations. *Physical Review Fluids*, *1*(1), 014301.

Bell, T. H. (1975). Topographically generated internal waves in open ocean. *Journal of Geophysical Research*, *80*, 320–327.

Bourget, B., Dauxois, T., Joubaud, S., & Odier, P. (2013). Experimental study of parametric subharmonic instability for internal plane waves. *Journal of Fluid Mechanics*, *723*, 1–20.

Buhler, O., & Muller, C. (2009). Saturation of the internal tides and induced mixing in the abyssal ocean. *Journal of Physical Oceanography*, *39*, 2077–209.

Buijsman, M. C., Klymak, J. M., Legg, S., Alford, M. H., Farmer, D., MacKinnon, J. A., et al. (2014). Three-dimensional double-ridge internal tide resonance in Luzon Strait. *Journal of Physical Oceanography*, *44*(3), 850–869.

de Lavergne, C., Falahat, S., Madec, G., Roquet, F., Nycander, J., & Vic, C. (2019). Toward global maps of internal tide energy sinks. *Ocean Modelling*, *137*, 52–75.

de Lavergne, C., Vic, C., Madec, G., Roquet, F., Waterhouse, A. F., Whalen, C. B., et al. (2020). A parameterization of local and remote tidal mixing. *Journal of Advances in Modeling Earth Systems*, *12*, e2020MS002065. https://doi.org/10.1029/2020MS002065

Dossmann, Y., Bourget, B., Brouzet, C., Dauxois, T., Joubaud, S., & Odier, P. (2016). Mixing by internal waves quantified using combined PIV/PLIF technique. *Experiments in Fluids*, *57*(8), 132.

Dossmann, Y., Gamble Rosevear, M., Griffiths, R. W., McC. Hogg, A., Hughes, G. O., & Copeland, M. (2016). Experiments with mixing in stratified flow over a topographic ridge. *Journal of Geophysical Research: Oceans*, *121*, 6961–6977. https://doi.org/10.1002/2016JC011990

Dossmann, Y., Paci, A., Auclair, F., & Floor, J. W. (2011). Simultaneous velocity and density measurements for an energy-based approach to internal waves generated over a ridge. *Experiments in Fluids*, *51*(4), 1013–1028.

Dossmann, Y., Shakespeare, C., & Hogg, A. M. (2020). Experimental data and linear model for "Asymmetric internal tide generation in the presence of a steady flow". https://doi.org/10.5281/zenodo.3889612

Dunphy, M., & Lamb, K. G. (2014). Focusing and vertical mode scattering of the first mode internal tide by mesoscale eddy interaction. *Journal of Geophysical Research: Oceans*, *119*, 523–536. https://doi.org/10.1002/2013JC009293

Falahat, S., Nycander, J., Roquet, F., & Zarroug, M. (2014). Global calculation of tidal energy conversion into vertical normal modes. *Journal of Physical Oceanography*, *44*(12), 3225–3244.

Gerkema, T., Maas, L. R. M., & van Haren, H. (2013). A note on the role of mean flows in Doppler-shifted frequencies. *Journal of Physical Oceanography*, *43*(2), 432–441.

Goff, J. A. (2010). Global prediction of abyssal hill root-mean-square heights from small-scale altimetric gravity variability. *Journal of Geophysical Research*, *115*, B12104. https://doi.org/10.1029/2010JB007867

Gregg, M. C., & Ozsoy, E. (1999). Mixing on the Black Sea shelf north of the Bosphorus. *Geophysical Research Letters*, *26*(13), 1869–1872.

Hacker, J., Linden, P. F., & Dalziel, S. B. (1996). Mixing in lock-release gravity currents. *Dynamics of Atmospheres and Oceans*, *24*, 183–195.

Joubaud, S., Munroe, J., Odier, P., & Dauxois, T. (2012). Experimental parametric subharmonic instability in stratified fluids. *Physics of Fluids*, *24*(4), 041,703.

Kiss, A. E., Hogg, A. M., Hannah, N., Boeira Dias, F., Brassington, G. B., Chamberlain, M. A., et al. (2020). ACCESS-OM2 v1. 0: A global ocean-sea ice model at three resolutions. *Geoscientific Model Development*, *13*(2), 401–442.

Kunze, E. (2017). Internal-wave-driven mixing: Global geography and budgets. *Journal of Physical Oceanography*, *47*(6), 1325–1345.

Lee, F. M., Allshouse, M. R., Swinney, H. L., & Morrison, P. J. (2018). Internal wave energy flux from density perturbations in nonlinear stratifications. *Journal of Fluid Mechanics*, *856*, 898–920.
MacKinnon, J. A., Alford, M. H., Sun, O., Pinkel, R., Zhao, Z., & Klymak, J. (2013). Parametric subharmonic instability of the internal tide at 29°N. *Journal of Physical Oceanography*, *43*(1), 17–28.
MacKinnon, J. A., Zhao, Z., Whalen, C. B., Waterhouse, A. F., Trossman, D. S., Sun, O. M., et al. (2017). Climate process team on internal wave-driven ocean mixing. *Bulletin of the American Meteorological Society*, *98*(11), 2429–2454.
Melet, A., Hallberg, R., Legg, S., & Polzin, K. (2013). Sensitivity of the ocean state to the vertical distribution of internal-tide-driven mixing. *Journal of Physical Oceanography*, *43*(3), 602–615.
Melet, A., Nikurashin, M., Muller, C., Falahat, S., Nycander, J., Timko, P. G., et al. (2013). Internal tide generation by abyssal hills using analytical theory. *Journal of Geophysical Research: Oceans*, *118*, 6303–6318. https://doi.org/10.1002/2013JC009212
Munk, W., & Wunsch, C. (1998). Abyssal recipes II: Energetics of tidal and wind mixing. *Deep Sea Research Part I: Oceanographic Research Papers*, *45*(12), 1977–2010.
Nikurashin, M., & Ferrari, R. (2010a). Radiation and dissipation of internal waves generated by geostrophic motions impinging on small-scale topography: Theory. *Journal of Physical Oceanography*, *40*, 1055–1074.
Nikurashin, M., & Ferrari, R. (2010b). Radiation and dissipation of internal waves generated by geostrophic motions impinging on small-scale topography: Application to the Southern Ocean. *Journal of Physical Oceanography*, *40*, 2025–2042.
Nikurashin, M., & Ferrari, R. (2011). Global energy conversion rate from geostrophic flows into internal lee waves in the deep ocean. *Geophysical Research Letters*, *38*, L08610. https://doi.org/10.1029/2011GL046576
Nikurashin, M., & Ferrari, R. (2013). Global energy conversion rate from geostrophic flows into internal lee waves in the deep ocean. *Geophysical Research Letters*, *40*, 3133–3137. https://doi.org/10.1029/2011GL046576
Nycander, J. (2005). Generation of internal waves in the deep ocean by tides. *Journal of Geophysical Research*, *110*, C10028. https://doi.org/10.1029/2004JC002487
Nycander, J. (2006). Tidal generation of internal waves from a periodic array of steep ridges. *Journal of Fluid Mechanics*, *567*, 415.
Polzin, K. L. (2009). An abyssal recipe. *Ocean Modelling*, *30*(4), 298–309.
Polzin, K. L., Toole, J. M., Ledwell, J. R., & Schmitt, R. W. (1997). Spatial variability of turbulent mixing in the abyssal ocean. *Science*, *276*(5309), 93–96.
Sarkar, S., & Scotti, A. (2017). From topographic internal gravity waves to turbulence. *Annual Review of Fluid Mechanics*, *49*, 195–220.
Shakespeare, C. J. (2020). Interdependence of internal tide and lee wave generation at abyssal hills: Global calculations. *Journal of Physical Oceanography*, *50*(3), 655–677. https://doi.org/10.1175/jpo-d-19-0179.1
Shakespeare, C. J., Arbic, B. K., & Hogg, A. M. (2020). The drag on the barotropic tide due to baroclinic motions. *Journal of Physical Oceanography*. https://doi.org/10.1175/JPO-D-19-0167.1
St. Laurent, L. C., Simmons, H. L., & Jayne, S. R. (2002). Estimating tidally driven mixing in the deep ocean. *Geophysical Research Letters*, *29*, 2106. https://doi.org/10.1029/2002GL015633
Sutherland, B. R., Lee, B., & Ansong, J. K. (2012). Light attenuation experiments on double diffusive plumes and fountains. *Physics of Fluids*, *24*, 066,605.
Todd, R. E. (2017). High-frequency internal waves and thick bottom mixed layers observed by gliders in the gulf stream. *Geophysical Research Letters*, *44*, 6316–6325. https://doi.org/10.1002/2017GL072580
Vic, C., Garabato, A. C. N., Green, J. A. M., Waterhouse, A. F., Zhao, Z., Melet, A., et al. (2019). Deep-ocean mixing driven by small-scale internal tides. *Nature Communications*, *10*(1), 1–9.
Yang, L., Nikurashin, M., Hogg, A. M., & Sloyan, B. M. (2018). Energy loss from transient eddies due to lee wave generation in the southern ocean. *Journal of Physical Oceanography*, *48*(12), 2867–2885.
Zhang, H. P., King, B., & Swinney, H. L. (2007). Experimental study of internal gravity waves generated by supercritical topography. *Physics of Fluids*, *19*(9), 096,602.
Zheng, K., & Nikurashin, M. (2019). Downstream propagation and remote dissipation of internal waves in the southern ocean. *Journal of Physical Oceanography*, *49*(7), 1873–1887.